Title	Investigation of particle breakage under one-dimensional compression of sand using X-ray microtomography
Authors(s)	Zhao, Budi, Wang, Jianfeng, Andò, Edward, et al.
Publication date	2020-05-05
Publication information	Zhao, Budi, Jianfeng Wang, Edward Andò, and et al. “Investigation of Particle Breakage under One-Dimensional Compression of Sand Using X-Ray Microtomography.” Canadian Science Publishing, May 5, 2020. https://doi.org/10.1139/cgj-2018-0548.
Publisher	Canadian Science Publishing
Item record/more information	http://hdl.handle.net/10197/12588
Publisher's version (DOI)	10.1139/cgj-2018-0548

An Investigation of Particle Breakage under One-Dimensional Compression of Sand Using X-ray Micro-Tomography

Budi Zhao[1], Jianfeng Wang[1,2], Edward Andò[3], Gioacchino Viggiani[3], Matthew R. Coop[4]

[1]City University of Hong Kong, Hong Kong, China

[2]Shenzhen Research Institute of City University of Hong Kong, Shenzhen, China

[3]Univ. Grenoble Alpes, CNRS, Grenoble INP, 3SR, F-38000 Grenoble, France

[4]University College London, London, United Kingdom

Abstract. Particle breakage alters particle-scale properties of granular soils including particle size, shape, and contact conditions, and changes macro-scale properties including soil compressibility, shear strength, and permeability. This study monitors the crushing of natural quartz sands under one-dimensional compression with in-situ X-ray tomography, i.e., X-ray scans during loading. We use the assembly-scale and particle-scale images to characterise particle failure patterns, e.g., chipping, major splitting and comminution. Image processing and analysis enable us to determine the failure patterns around the yield stress, and the influence of initial density and particle morphology on the particle survival probability. We further quantify the degree of particle breakage with fractal dimension, breakage factor, and specific surface. Particle shape and coordination number both show a scale-dependent evolution pattern.

Keywords: fractals; laboratory tests; particle crushing/crushability; particle-scale behaviour; sands

Submit to: Canadian Geotechnical Journal (Technical Note)

Corresponding Author: Jianfeng Wang (jefwang@cityu.edu.hk)

1. Introduction

Particle breakage in granular materials is relevant to many geotechnical infrastructures, such as offshore piles (Randolph 1988), high rock-fill dams (Sowers et al. 1965) and railway ballast (Indraratna et al. 1998). In a granular assembly, individual particles serve as the structural units with inherent properties, e.g., mineralogy, morphology, and strength. A particle will break into a few pieces once its internal stress reaches the particle failure strength. At the micro-scale, particle breakage changes inter-particle contact conditions, and material fabrics, leading to local stress redistribution. At the macro-scale, particle breakage alters soil compressibility (Pestana and Whittle 1995), shear strength (Marsal 1967), dilatancy (Yamamuro and Lade 1996) and permeability (Lade et al. 1996).

X-ray micro-computed tomography (μCT) is a non-destructive imaging tool, i.e., it does not alter the internal structure during the testing process. The high resolution of μCT images has allowed investigations into particle-scale properties of sands, including inter-particle contact conditions (Hasan and Alshibli 2010; Andò et al. 2013; Druckrey et al. 2016; Wiebicke et al. 2017; Afshar et al. 2018), particle morphology/material fabrics (Fonseca et al. 2012 and 2013), the evolution of particle breakage (Cil and Alshibli 2014; Alikarami et al. 2014; Karatza et al. 2017; Guida et al. 2018; Alam et al. 2018), and particle kinematics (Hall et al. 2010; Andò et al. 2012).

This experimental study uses X-ray μCT to characterise the particle breakage behaviour within an assembly of sand particles which is subjected to one-dimensional compression. We collect five scans at predetermined stress levels and apply image processing and analysis methods to quantify survival probability, failure pattern, and the evolution of particle size, shape, and coordination number.

2. Experimental Methods

2.1. Mini Oedometer Apparatus

The mini oedometer apparatus, which was fabricated to allow high-resolution laboratory CT scanning during the loading process, has a two-layer specimen chamber made of X-ray transparent carbon fibre reinforced polymer with high stiffness and strength, as shown in Fig. 1a. The external chamber bears the reaction force, while the internal floating ring provides lateral confinement and remains mobile relative to both loading platens. The loading platens are made of ceramic with low density to reduce the X-ray attenuation contrast and high hardness to avoid indentation of the platens. The cell body includes a stepping motor to apply the vertical load, and a load cell and an LVDT to monitor axial load and displacement, respectively. The controlling and monitoring system of the apparatus is located outside of the scanner and is not interrupted during scanning.

2.2. Materials and Tests

The Leighton Buzzard sand (LBS) with a particle diameter range of 0.6 – 1.18 mm was used in this study. LBS is mainly composed of quartz and contains relatively round and smooth particles. A detailed investigation of the single particle crushing behaviour of LBS particles was previously carried out by the authors (Zhao et al. 2015).

Loose and dense specimens of a diameter 6 mm were prepared within the floating ring through slow deposition and layer-by-layer compaction, respectively. The specimens were then compressed at a constant rate of 1.8 mm/h and scanned at five predetermined stress levels: S1 (1 MPa) – at the initial loading, S2 (10 MPa) – around the yield stress, and S3-S5 (14, 19 and 28 MPa) – during post-yield compression, as shown in Fig. 1b. The yield stress σ_y is defined as the point with the maximum curvature in the *e*-log *σ* curve for the loose specimen and is approximately taken as 10 MPa. For each scan, we paused the loading and waited for about ten minutes to allow the specimen to stabilise.

In this study, we used a commercial scanner Phoenix v|tome|x located at General Electric Company, Shanghai, China, and a custom-built scanner RX-Solutions at Laboratoire 3SR, Grenoble, France. They both have a high-power cone-beam source, a high-resolution detector, and a precision rotation stage. We performed tests on loose and dense specimens, LBS-L-S and LBS-D-S, in Shanghai with a voxel size of 4.0 μm. A duplicate test is performed on a loose specimen, LBS-L-G, in Grenoble with a voxel size of 5.5 μm.

2.3. Image Processing and Analysis

The processing and analysis of tomography images include three major steps. First, we classified the voxels of the filtered images into different phases, i.e., air, carbon fibre, sand particles, and ceramic platens, based on the threshold values determined by the multiple Otsu method (Liao et al. 2001). Second, we identified individual particles and fragments and labelled them with different integers. Finally, we quantified the 3D morphology of individual particles/fragments with a series of characteristic parameters. More details of the image processing can be found in Zhao and Wang (2016).

Figure 2 shows the labelled particles in LBS-L-S at S1 and S5. The image processing resulted in an overall satisfactory identification of individual particles before and after extensive fragmentation. However, difficulties arose in segmenting tiny fragments and accurately evaluating their shape parameters. Some tiny fragments remain very close to each other with a separation distance less than a few voxels especially near contacts, as shown by the grey-value vertical slices at high-stress levels in Fig. 3. Therefore, we excluded fragments with a volume smaller than 0.001

mm^3 (about 6000 voxels) from further analysis. Note that the total volume of particles has a relative error < 2.1% for all stress levels.

Following Zhao and Wang (2016), the particle size parameters include volume V, surface area SA and three principal dimensions ($a \geq b \geq c$). Particle volume was used due to its lower dependency on particle shape. Two aspect ratios were used for a 3D particle, i.e., elongation index (EI= b/a) and flatness index (FI= c/b). The representative aspect ratio was defined as AR= (EI+FI)/2. The 3D mean-curvature roundness index R_{M} was evaluated at particle corners based on local mean curvatures. Particle compactness is quantified with two parameters, i.e., sphericity $\mathrm{S} = \sqrt[3]{36\pi V^2}/SA$ and convexity $\mathrm{C_X}$= V/V_{CH}, where V_{CH} is the volume of particle's convex hull.

2.4. Coordination Number

We measured the coordination number (CN) for each particle using the algorithm described in Andò (2013) and Andò et al. (2013). The algorithm’s accuracy mainly depends on the accuracy of particle segmentation (Jaquet et al. 2013; Wiebicke et al. 2017). It should be mentioned that the algorithm considers multiple contact points between two particles (if existing) as one contact point, and the contacts with the loading platens and floating oedometer ring are not considered.

3. Experimental Results

3.1. Failure Patterns at Assembly- and Particle-Scale

We describe particle-scale failures with chipping, splitting, and comminution (see illustrating sketches in Fig. 3). Chipping refers to minor parts split away from the particle, while splitting indicates the particle splits into two or more major pieces. Comminution describes the extensive fragmentation resulting from a series of failure events.

Figure 3 shows the scan-by-scan comparison between the vertical slices of LBS-L-S at different stress levels, which identifies two chipping failures (S1-S2), two splitting failures of elongated particles and three chipping failures (S2-S3), and extensive fragmentation, and comminution (S3-S5). The fragments remained in proximity to each other, especially for the dense specimen.

Figure 4 illustrates the particle-scale failure patterns with four particles. Particle A experiences a progressive failure as the stress increases. First, a fracture initiates from the lower contact, propagates to a close concave feature and results in a chipping failure (A-S3). The conchoidal fracture occurs since the quartz particle has no cleavage. Then, a splitting failure occurs by a fracture connecting two contact points and generates a few fragments around the contact points (A-S4). Finally, the comminution of existing fragments generates many fragments with varying particle size and shape (A-S5).

Particles B and C with elongated morphology fail in bending as suggested by the cantilever curls. The fractures initiate at the tensile sides (marked by an arrow), then slow down and change direction at the tensile/compression boundary. A concave feature serves as a surface weakness and the fracture initiation point (C-S2). A small amount of LBS particles (<1%) have initial internal voids, which may also affect the fracture patterns (particle D). These typical examples demonstrate the varying particle failure patterns, which differ from the single particle crushing pattern under two flat platens (Zhao et al. 2015).

3.2. *Volume-Change Ratio of Crushed Particles at S2*

Visual inspection method (VIM) identified 68 initial particles that crushed into 177 fragments at S2 from the labelled images of three specimens, as illuastrated in the Appendix. The vertical stress values at S2 are 9.51 MPa, 9.70 MPa and 10.72 MPa for LBS-L-S, LBS-D-L, and LBS-L-G, respectively. Most crushing events (~ 85%) generate two or three fragments. A volume-change ratio is defined as $R_V = (V_0\text{-}V_1)/V_0$, where V_0 is the mother particle volume, and V_1 is the volume of its largest fragment. Fig. 5a illustrates the volume-change ratio with the 3D view of four particle failure patterns. Fig. 5b shows the cumulative distribution of R_V for loose and dense specimens. The loose specimens have about 10% particles crushed with R_V up to 0.65, while the dense specimen has only about 4% particles crushed with R_V up to 0.23. Note that a fragment tracking algorithm is needed to analyse a large number of failure events in the post-yield scans.

3.3. *Particle Survival Probability*

We used the labelled images to inspect visually the intactness of initial particles in the following scans to determine their survival probability. This analysis considers only major splitting and excludes chipping failures. The reduction of survival probability can be described in two stages: Stage-1, a small percentage of particles crush up to 3% strain level (around σ_y); Stage-2, the survival probability reduces linearly with the strain level, and about 50% particles fail at the highest strain level (Fig. 6a). Cil and Alshibli (2014) reported similar results in oedometer tests on brittle silica sand particles (d~ 0.7 mm) using X-ray CT images and discrete element simulation. Their numerical results agree well with our experiments for both loose and dense specimens (Fig. 6a). A similar level of particle failure percentage leads to a lower vertical strain in the denser specimen. The lower deformability in a denser specimen is mainly attributed to the fact that the particles surrounding a crushing event have a higher chance to reconstitute a skeleton. The skeleton formation may also reduce the possibility of further comminution of the existing fragments (e.g., A-S5 in Fig. 4).

We group the initial particles according to their shape parameters and evaluate their survival probability at the highest stress level (S5). Each group contains more than twenty particles for a reliable statistical analysis. The particles with lower aspect ratio, sphericity and convexity are more likely to experience major splitting failure (Fig. 6b). For example, the particles with AR=0.85 and 0.6 have a survival probability of 69% and 22%, respectively. Conversely, the influence of particle roundness on failure probability is not obvious due to two major reasons: (1) R_{M} is an overall roundness index, which reflects poorly the morphology at contacts; and (2) chipping failures are not considered in evaluating survival probability.

3.4. Particle Size Distribution

The cumulative particle size distribution (PSD) changes slightly from S1 to S4 and more extensively from S4 to S5 (Fig. 7a). The frequency PSDs from different scans intersect at the point of V= 0.16 mm^3, as shown in Fig. 7b, suggesting that the continuous fragmentation of various sized particles produces a balance of volume change at that point. The fragments smaller than the minimum initial particle (0.1 mm^3) form a fractal distribution: $N(>V)\sim V^{-D/3}$, where $N(>V)$ is the number of fragments larger than V (Fig. 7c). The fractal dimension D increases almost linearly with the vertical stress in a semi-log plot after S2 (Fig. 7d).

3.5. Breakage Factor and Specific Surface

The breakage factor B_{f}, which was defined by Nakata et al. (1999) as the volume ratio of particles smaller than the minimum particle size in the original specimen (0.1 mm^3), was adopted to quantify the particle breakage degree, as shown in Fig. 8a. The curve shows a distinct bilinear pattern, with the turning point located around the yield stress. The dense specimen generates a smaller amount of fines and a lower B_f value at the maximum stress level than the loose specimens.

In addition to the breakage factor, the specific surface is another important parameter suitable for the measurement of particle breakage degree and often used in the constitutive modelling of crushable sands (e.g., McDowell et al. 1996; Russell, 2011). In this study, the specific surface is estimated based on μCT data as $S_s = \mathrm{SA}/(V \cdot \rho)$, where ρ is the quartz density (2.65 g/cm^3). Similar to the approach adopted by Zhao et al. (2015), we used a fractal-based method to estimate the surface area of the fragments between 0.001 and 10^{-12} mm^3 by assuming the sphericity to be the average sphericity of the fragments smaller than 0.1 mm^3 (Fig. 9c). These fragments contribute to about 10% of the total surface area at the maximum stress level. The three specimens have an initial specific surface $S_{s0} \sim 3$ m^2/kg, which is equivalent to a sphere with $d = 0.75$ mm (Fig. 8b). S_s remains almost constant before S2 and increases gradually to about $1.5S_{s0}$ at the maximum stress level (about $2.8\sigma_y$).

3.6. Particle Shape

Particle shape shows a scale-dependent evolution: larger fragments evolve towards a cube with higher particle form and lower roundness, while smaller fragments are more flat (Fig. 9). The mean values of S and C_X remain almost constant for smaller fragments, due to the opposite trends of AR and R_M. This constant sphericity also exists for the fragments generated in single particle crushing tests (Zhao et al. 2015). We compare the 3D shape evolution with the 2D quantification results in a similar experiment on 1-2 mm LBS particles from Altuhafi and Coop (2011). Both 2D and 3D results reflect the reduction of particle form, sphericity, and convexity.

3.7. Coordination Number

The evolving particle size distribution alters the coordination number (CN) for different-sized particles. As shown in Fig. 10a, the average CN for particles of a given size increases significantly with the increasing particle breakage within the specimen, and such a trend is much more pronounced for larger particles. This is because a great number of smaller fragments generated fill the voids and surround the larger particles. At the highest stress level (i.e., S5), it is evident that the CN vs V plot reaches a fractal distribution: $\mathrm{CN}(>V) = 21V^{-0.33}$. The fractal dimension equals 0.99, which is slightly larger than the fractal dimension for PSD (D= 0.9). De Bono and McDowell (2016) reported a similar trend with a larger fractal dimension ~1.7 from numerical simulations.

A large number of smaller fragments fill the voids and have low CN values. As a result, the average CN for all the particles throughout the compression process remains nearly constant at 6, as shown in Fig. 10b. To reflect better the influence of particle volume on the CN during the compression process, we plotted the volume-weighted average CN, which was calculated by multiplying each particle's CN by its volume (as a weighting factor), against the applied vertical stress in Fig. 10b. The curve shows again a bilinear pattern with a sharp increase of CN from S2.

4. Conclusions

This experimental study explores the particle breakage behaviour within an assembly of LBS particles under one-dimensional compression using X-ray μCT. The major thrust of this study lies in its comprehensive analysis of a variety of particle-scale properties based on μCT data, unveiling the microscopic origin of the macroscopic mechanical behaviour, particularly the bilinear pattern of the stress-strain curve, yielding, and post-yield rapid compression. In detail, the following conclusions can be drawn from this study:

- In a sand assembly, particle morphology and multiple contacts lead to the complexity and variety of particle failure patterns. For example, elongated particles are more likely to fail with bending failures. Contacts and surface/internal flaws are prone to experience stress concentration and serve as crack initiation points.
- The consistent patterns of the fractal dimension, breakage factor, specific surface and volume-weighted CN versus the applied vertical stress demonstrate that these parameters work well to reflect the geometric nature of sand fragmentation and fabric evolution during particle breakage.
- A dense specimen has initially a lower failure probability and less extensive failure modes (smaller Rv) than a loose specimen around the yield stress. The influence of initial density on particle survival probability diminishes after substantial particle breakage. However, a particle failure event leads to higher compression in a loose specimen and generates more fines through further comminution of existing fragments.
- Particle shape and coordination number both show a scale-dependent evolution. Larger particles evolve towards a cubic shape with high CN, while smaller fragments are flatter and floating with a small CN. The scale-dependent evolution reflects the different loading conditions and failure modes for coarse and fine particles.

Acknowledgements

The study presented in this article was supported by General Research Fund No. CityU 11272916 and CityU 11213517 from the Research Grant Council of the Hong Kong SAR and Research Grant No. 51779213 from the National Science Foundation of China. Laboratoire 3SR is part of the LabEx Tec21 (Investissements d'Avenir - grant agreement nANR-11-LABX-0030).

References

Afshar, T., Disfani, M.M., Narsilio, G.A., and Arulrajah, A. 2018. Post-breakage changes in particle properties using synchrotron tomography. *Powder Technology*, **325**: 530–544.

Alikarami, R., Andò, E., Gkiousas-Kapnisis, M., Torabi, A., and Viggiani, G. 2014. Strain localisation and grain breakage in sand under shearing at high mean stress: insights from in situ X-ray tomography. *Acta Geotechnica*, **10**(1): 15–30.

Altuhafi, F.N. and Coop, M.R. 2011. Changes to particle characteristics associated with the compression of sands. *Géotechnique*, **61**(6): 459–471.

Andò, E. 2013. Experimental investigation of microstructural changes in deforming granular media using x-ray tomography. PhD thesis, Université de Grenoble.

Andò, E., Hall, S.A., Viggiani, G., Desrues, J., and Bésuelle, P. 2012. Grain-scale experimental investigation of localised deformation in sand: a discrete particle tracking approach. *Acta Geotechnica*, **7**(1): 1–13.

Andò, E., Viggiani, G., Hall, S., and Desrues, J. 2013. Experimental micro-mechanics of granular media studied by X-ray tomography: recent results and challenges. *Géotechnique Letters*, **3**(July-September): 142–146.

Cil, M.B. and Alshibli, K.A. 2014. 3D evolution of sand fracture under 1D compression. *Géotechnique*, **64**(5): 351–364.

de Bono, J.P. and McDowell, G.R. 2016. The fractal micro mechanics of normal compression. *Computers and Geotechnics*, **78**: 11–24.

Druckrey, A.M., Alshibli, K.A., and Al-Raoush, R.I. 2016. 3D characterization of sand particle-to-particle contact and morphology. *Computers and Geotechnics*, **74**: 26–35.

Fonseca, J., O'Sullivan, C., Coop, M.R., and Lee, P.D. 2012. Non-invasive characterization of particle morphology of natural sands. *Soils and Foundations*, **52**(4): 712–722.

Fonseca, J., O'Sullivan, C., Coop, M.R., and Lee, P.D. 2013. Quantifying the evolution of soil fabric during shearing using directional parameters. *Géotechnique*, **63**(6): 487–499.

Guida, G., Casini, F., Viggiani, G.M.B., Andò, E., and Viggiani, G. 2018. Breakage mechanisms of highly porous particles in 1D compression revealed by X-ray tomography. *Géotechnique Letters*, **8**(2): 155-160.

Hagerty, M.M., Hite, D.R., Ullrich, C.R., and Hagerty, D.J. 1993. One-dimensional high-pressure compression of granular media. *Journal of Geotechnical Engineering*, **119**(1): 1–18.

Hall, S. A., Bornert, M., Desrues, J., Pannier, Y., Lenoir, N., Viggiani, G., and Bésuelle, P. 2010. Discrete and continuum analysis of localised deformation in sand using X-ray µCT and volumetric digital image correlation. *Géotechnique*, **60**(5): 315–322.

Hasan, A. and Alshibli, K.A. 2010. Experimental assessment of 3D particle-to-particle interaction within sheared sand using synchrotron microtomography. *Géotechnique*, **60**(5): 369.

Indraratna, B., Ionescu, D., and Christie, H. 1998. Shear behavior of railway ballast based on large-scale triaxial tests. *Journal of geotechnical and geoenvironmental Engineering*, **124**(5): 439–449.

Jaquet, C., Andò, E., Viggiani, G., and Talbot, H. 2013. Estimation of separating planes between touching 3d objects using power watershed. *In International Symposium on Mathematical Morphology and Its Applications to Signal and Image Processing*, 452–463. Springer.

Karatza, Z., Andò, E., Papanicolopulos, S., Ooi, J., and Viggiani, G. 2017. Evolution of deformation and breakage in sand studied using x-ray tomography. *Géotechnique*, **1**: 1–11.

Lade, P.V., Yamamuro, J.A., and Bopp, P.A. 1996. Significance of particle crushing in granular materials. *Journal of Geotechnical Engineering*, **122**(4): 309–316.

Marsal, R.J. 1967. Large-scale testing of rockfill materials. *Journal of the Soil Mechanics and Foundations Division*, **93**(2): 27–43.

McDowell, G., Bolton, M., and Robertson, D. 1996. The fractal crushing of granular materials. *Journal of the Mechanics and Physics of Solids*, **44**(12): 2079–2101.

Alam, M.F., Haque, A., Ranjith P.G. 2018. A study of the particle-level fabric and morphology of granular soils under one-dimensional compression using insitu x-ray CT imaging. *Materials*, **11**(6): 919.

Nakata, Y., Hyde, A., Hyodo, M., and Murata, H. 1999. A probabilistic approach to sand particle crushing in the triaxial test. *Géotechnique*, **49**(5): 567–583.

Pestana, J.M. and Whittle, A. 1995. Compression model for cohesionless soils. *Géotechnique*, **45**(4): 611–631.

Randolph, M.F. 1988. The axial capacity of deep foundations in calcareous soil. *In Proc. Int. Conf. Calcareous Sediments*, **2**: 837–857.

Russell, A.R. 2011. A compression line for soils with evolving particle and pore size distributions due to particle crushing. *Géotechnique Letters*, **1**(January-March): 5–9.

Sowers, G.F., Williams, R.C., and Wallace, T.S. 1965. Compressibility of broken rock and the settlement of rockfills. *In Proc. 6th ICSMFE*, **2**: 561–565.

Wiebicke, M., Andò, E., Herle, I., and Viggiani, G. 2017. On the metrology of interparticle contacts in sand from x-ray tomography images. *Measurement Science and Technology*, **28**(12): 124007.

Yamamuro, J.A. and Lade, P.V. 1996. Drained sand behavior in axisymmetric tests at high pressures. *Journal of Geotechnical Engineering*, **122**(2): 109–119.

Zhao, B. and Wang, J. 2016. 3D quantitative shape analysis on form, roundness, and compactness with μCT. *Powder Technology*, **291**: 262–275.

Zhao, B., Wang, J., Coop, M.R., Viggiani, G., and Jiang, M. 2015. An investigation of single sand particle fracture using x-ray micro-tomography. *Géotechnique*, **65**(8): 625–641.

Figure List

- Fig. 1. The radiographs of specimen chamber (a) and the compression curves (b).
- Fig. 2. Labelled images for LBS-L-S at the initial loading state (S1) and the highest stress level (S5).
- Fig. 3. Grey-level vertical slices of LBS-L-S at multiple stress levels and of LBS-D-S at the highest stress level. Sketches illustrate different failure modes. Note: blue dots identify scan-by-scan failure events, and red circles indicate the particles used to illustrating failure modes.
- Fig. 4. Illustration of particle-scale failure modes. Particle A: progressive failure. Particles B and C: bending failures of elongated particles. Particle D: internal void related failure. Note: CL – cantilever curl; black circles mark fracture initiation locations.
- Fig. 5. (a) 3D view of failure patterns with varying volume-change ratios. (b) Cumulative failure percentage concerning R_V in the loose and dense specimens at S2 (~10 MPa).
- Fig. 6. (a) Evolution of survival probability with the increasing vertical strain. The results of the discrete element method DEM simulations on loose and dense specimens are from Cil and Alshibli (2014). (b) Influence of particle morphology on the survival probability at the highest stress level (S5).
- Fig. 7. Evolution of particle size distribution for LBS-L-S: (a) cumulative PSD; (b) frequency PSD; (c) fractal distribution of cumulative particle number. (d) Evolution of fractal dimension with the increasing vertical stress.
- Fig. 8. Evolution of the breakage factor (a) and the specific surface (b) with the increasing vertical stress. Note: the specific surfaces for a quartz sphere with varying diameters are marked by the blue lines in (b).

- Fig. 9. Scale-dependent evolution of particle shape parameters for LBS-L-S: (a) aspect ratio AR; (b) roundness R_M; (c) sphericity S; (d) convexity C_X. The data of G1 are 2D quantification results on LBS particles (1-2 mm) before and after a one-dimensional compression of 30 MPa (from Altuhafi and Coop, 2011). Note: arrows indicate the morphology evolution for initial-sized particles, and the dashed lines represent the trend curves for small fragments at the highest stress level.
- Fig. 10. Scale-dependent evolution of coordination number in LBS-L-S (a), and the evolution of average CN and volume-weighted average CN (V) with the increasing vertical stress (b).

Appendix: Visual Inspection Method (VIM)

Visual inspection method (VIM) compares slice-by-slice the 3D labelled images in which particles are represented with distinctive integers to associate crushed particles with their fragments. For example, LBS-L-S initially has 308 particles in S1. VIM identified 28 crushed particles with 75 associated fragments from S1 to S2. Fig. A-1 compares the 3D view of these particles before and after crushing. We quantified their failure patterns with the volume-change ratios (R_V) using the 3D volume of mother particles and the largest fragments. It shows that VIM performs well to identify crushing events in the current study. However, the efficiency of this method limits its application to a larger number of particles and fragments.

Fig. A-1. 3D view of particle crushing events from S1 to S2 in LBS-L-S together with volume-change ratios.

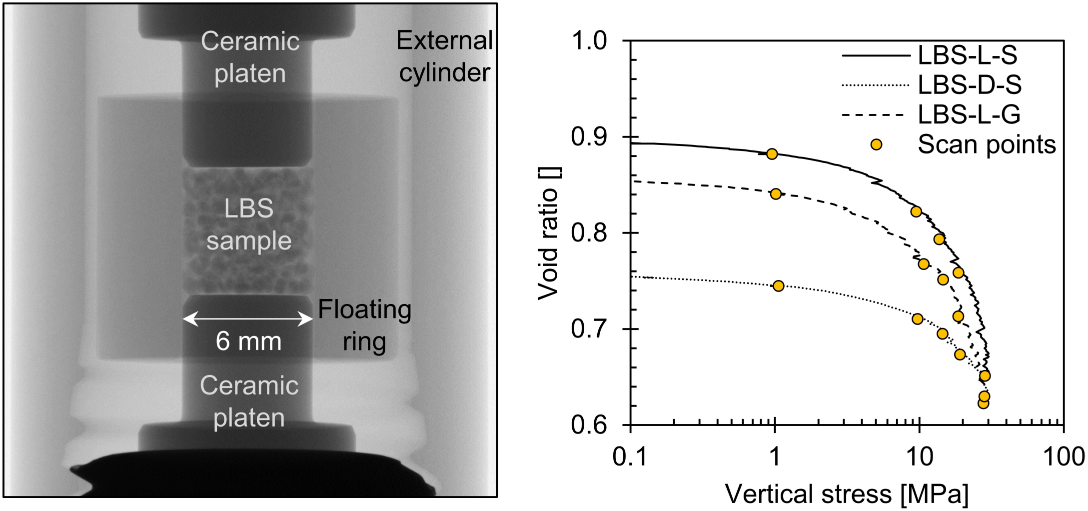

(a) **(b)**

Fig. 1. The radiographs of specimen chamber (a) and the compression curves (b).

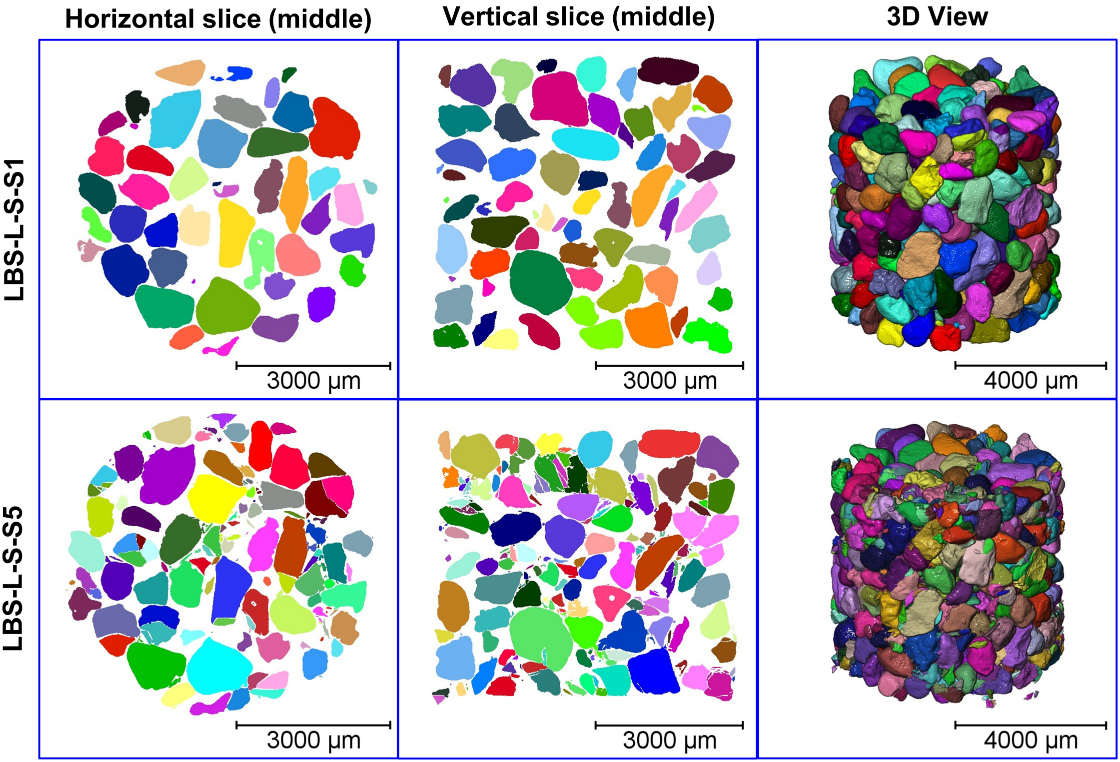

Fig. 2. Labelled images for LBS-L-S at the initial loading state (S1) and the highest stress level (S5).

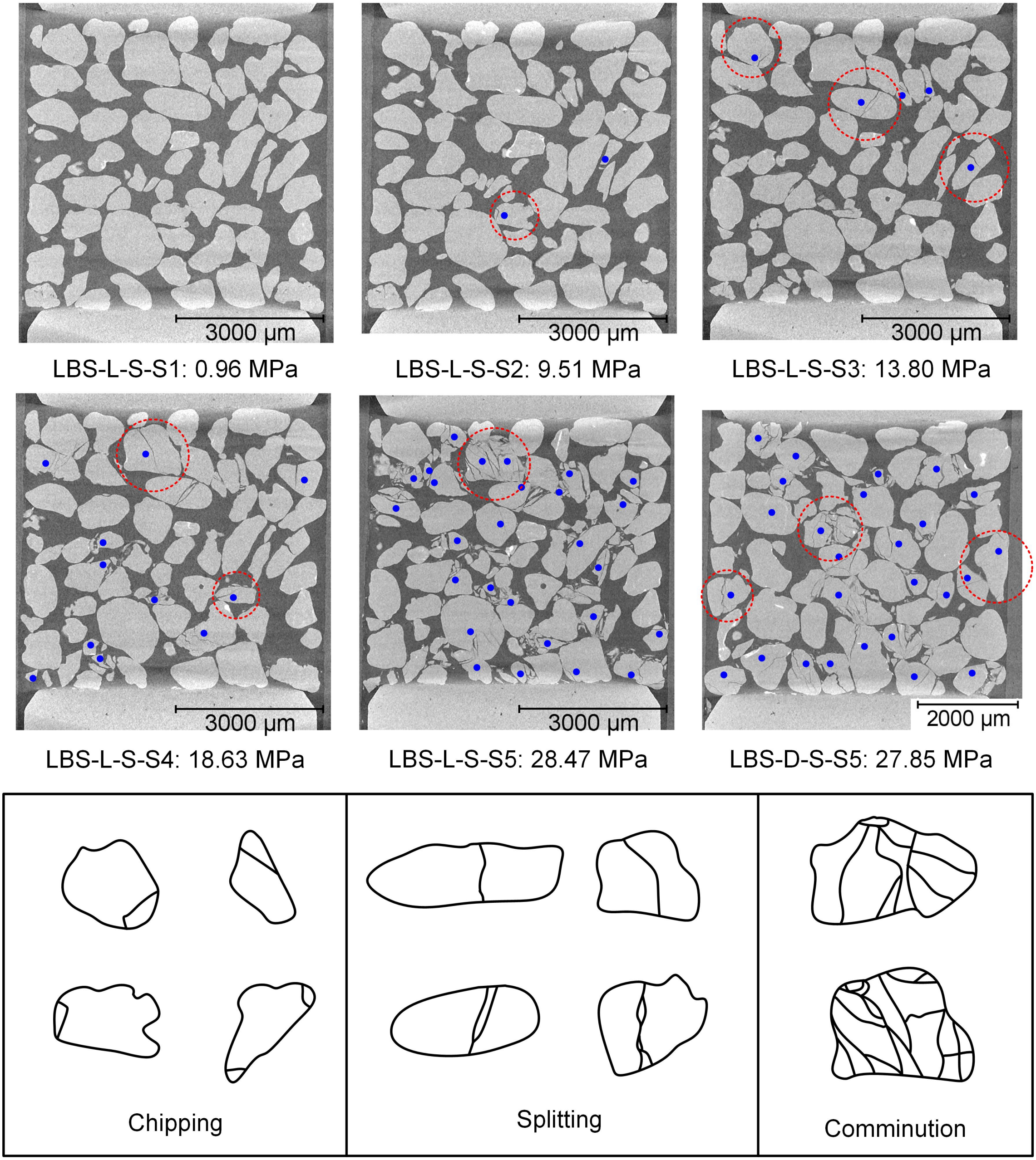

LBS-L-S-S1: 0.96 MPa

LBS-L-S-S2: 9.51 MPa

LBS-L-S-S3: 13.80 MPa

LBS-L-S-S4: 18.63 MPa

LBS-L-S-S5: 28.47 MPa

LBS-D-S-S5: 27.85 MPa

Fig. 3. Grey-level vertical slices of LBS-L-S at multiple stress levels and of LBS-D-S at the highest stress level. Sketches illustrate different failure modes. Note: blue dots identify scan-by-scan failure events, and red circles indicate the particles used to illustrating failure modes.

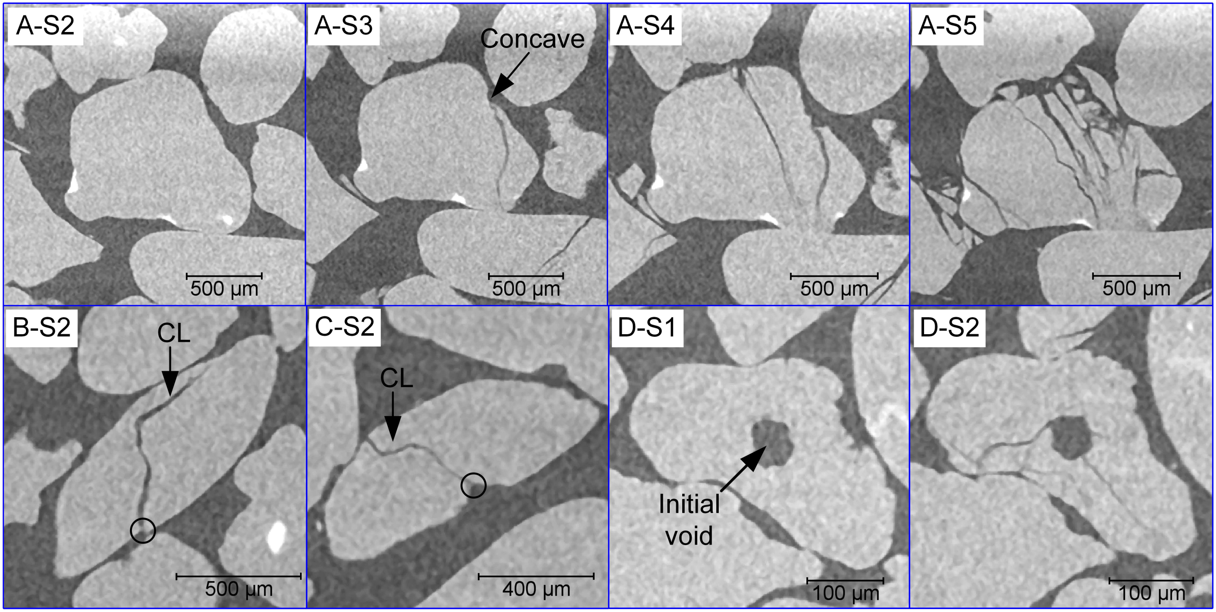

Fig. 4. Illustration of particle-scale failure modes. Particle A: progressive failure. Particles B and C: bending failures of elongated particles. Particle D: internal void related failure. Note: CL – cantilever curl; black circles mark fracture initiation locations.

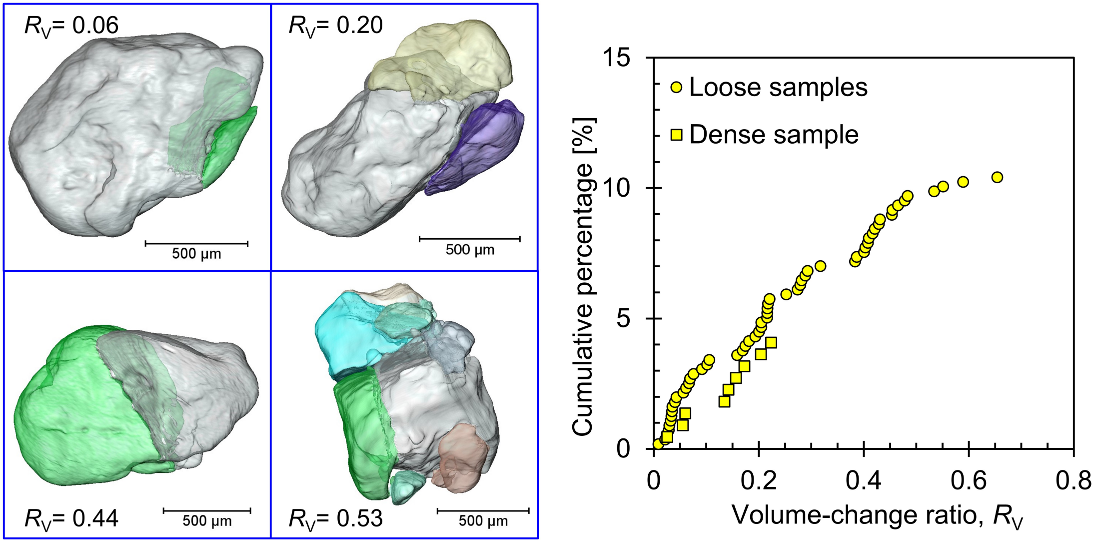

(a) **(b)**

Fig. 5. (a) 3D view of failure patterns with varying volume-change ratios. (b) Cumulative failure percentage concerning R_V in the loose and dense specimens at S2 (~10 MPa).

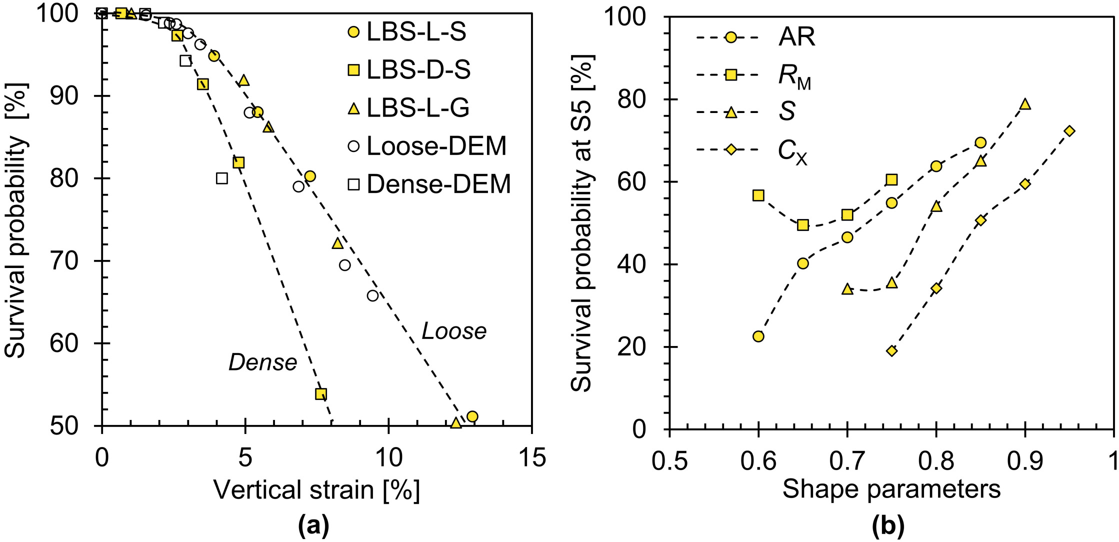

Fig. 6. (a) Evolution of survival probability with the increasing vertical strain. The results of the discrete element method DEM simulations on loose and dense specimens are from Cil & Alshibli (2014). (b) Influence of particle morphology on the survival probability at the highest stress level (S5).

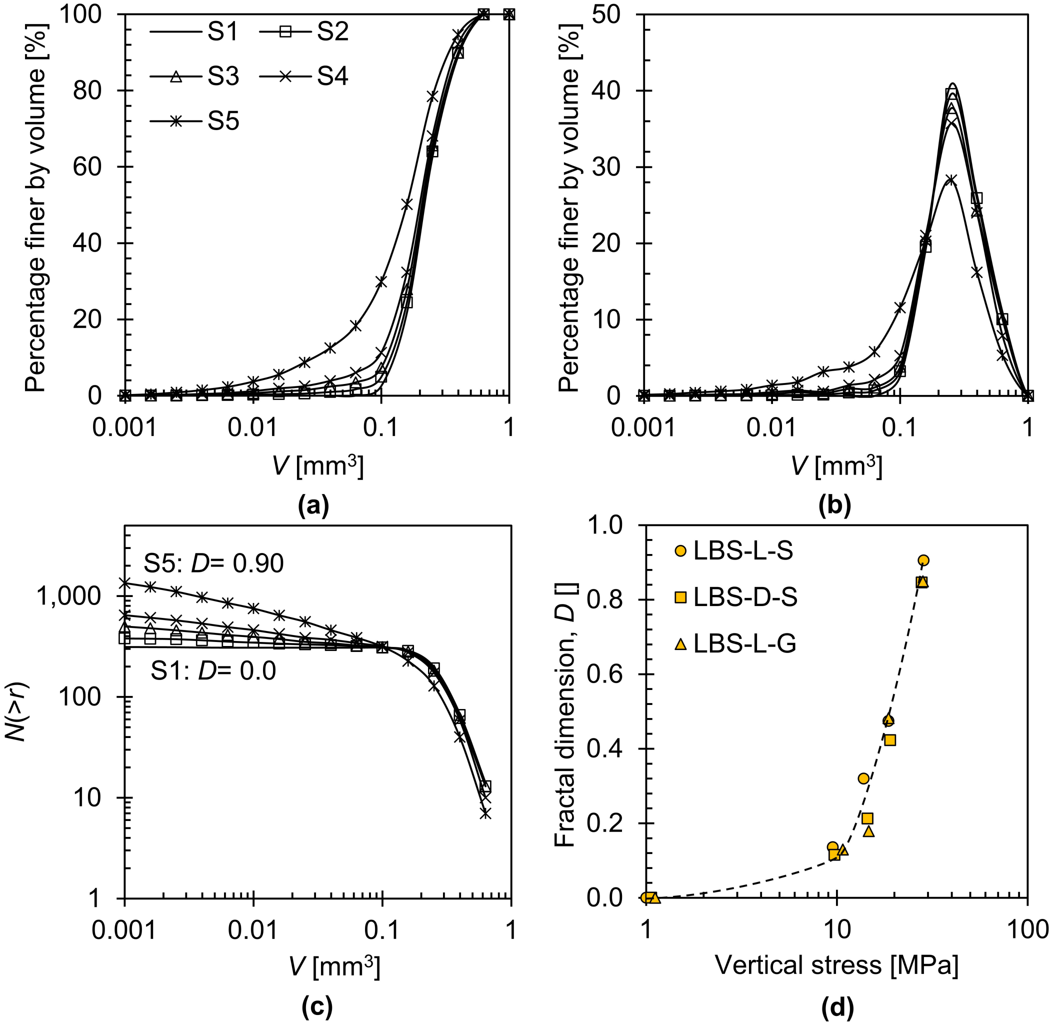

Fig. 7. Evolution of particle size distribution for LBS-L-S: (a) cumulative PSD; (b) frequency PSD; (c) fractal distribution of cumulative particle number. (d) Evolution of fractal dimension with the increasing vertical stress.

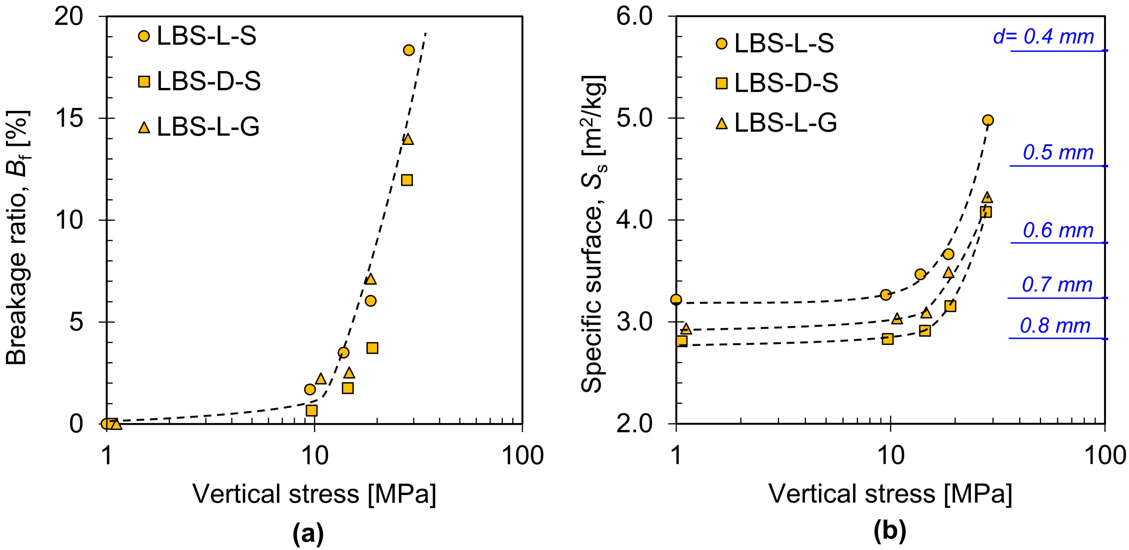

Fig. 8. Evolution of the breakage factor (a) and the specific surface (b) with the increasing vertical stress. Note: the specific surfaces for a quartz sphere with varying diameters are marked by the blue lines in (b).

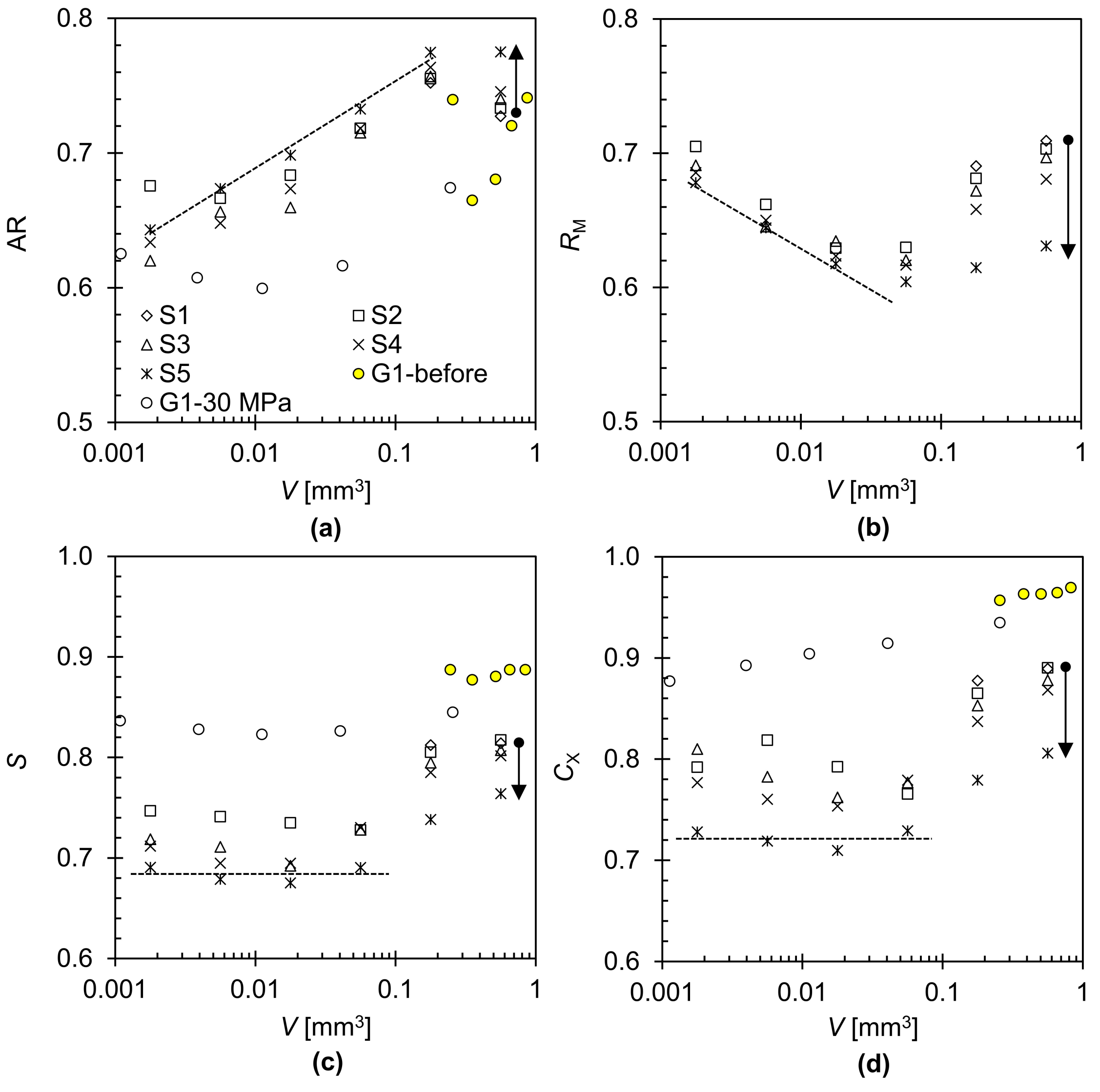

Fig. 9. Scale-dependent evolution of particle shape parameters for LBS-L-S: (a) aspect ratio AR; (b) roundness R_M; (c) sphericity S; (d) convexity C_X. The data of G1 are 2D quantification results on LBS particles (1-2 mm) before and after a one-dimensional compression of 30 MPa (from Altuhafi & Coop, 2011). Note: arrows indicate the morphology evolution for initial-sized particles, and the dashed lines represent the trend curves for small fragments at the highest stress level.

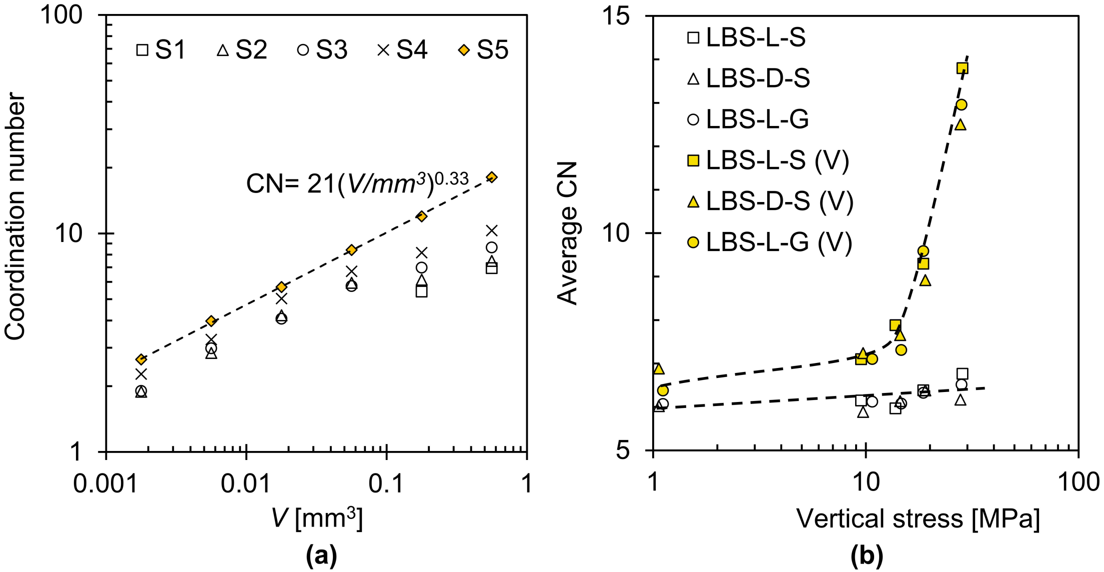

Fig. 10. Scale-dependent evolution of coordination number in LBS-L-S (a), and the evolution of average CN and volume-weighted average CN (V) with the increasing vertical stress (b).

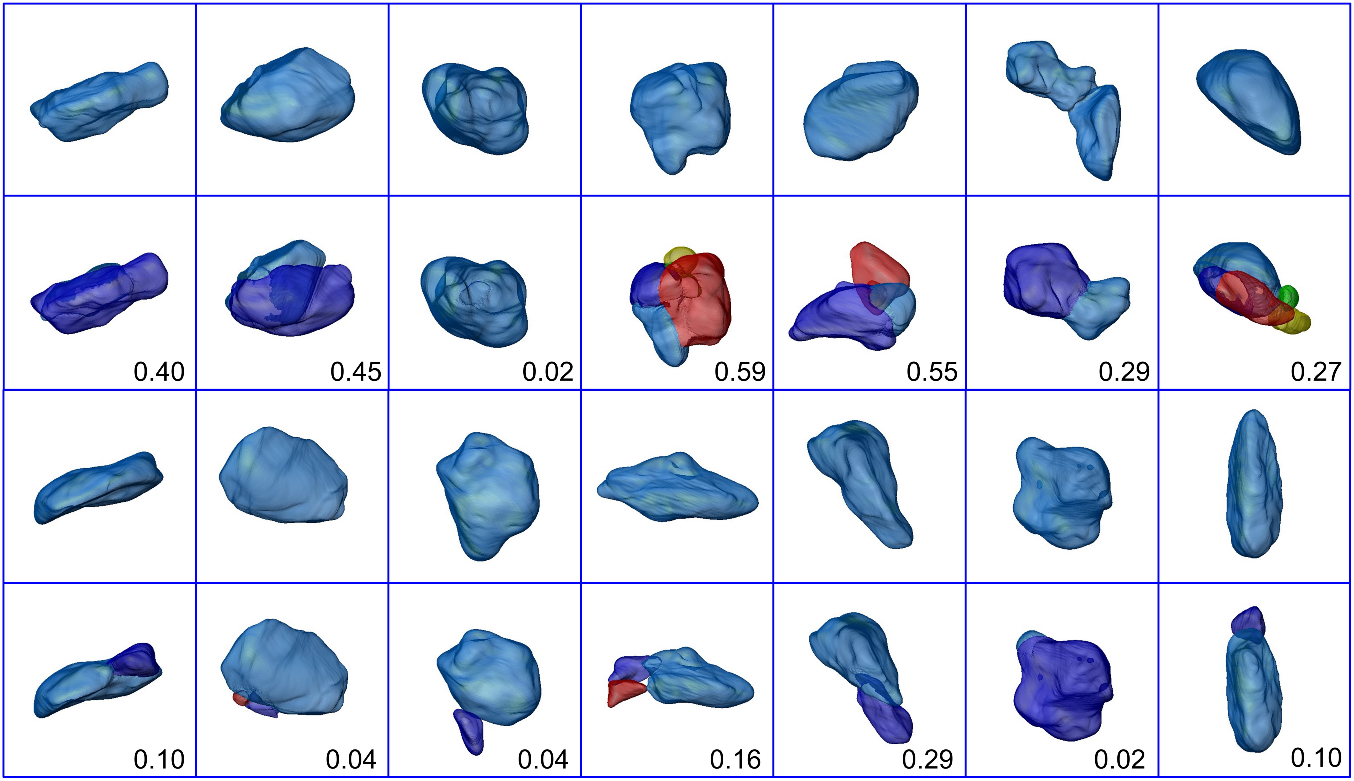

Fig. A-1. 3D view of particle crushing events from S1 to S2 in LBS-L-S together with volume-change ratios.

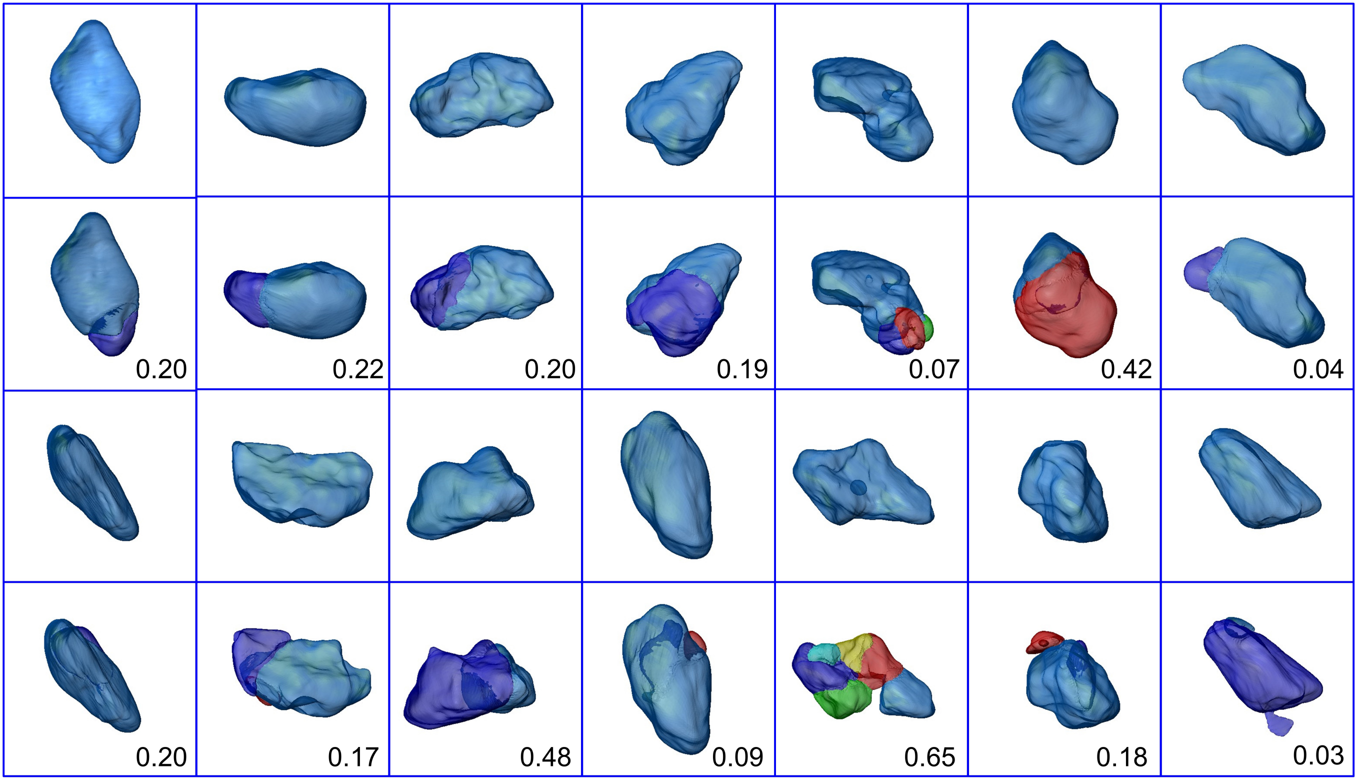

Fig. A-1. Continued.